PNAS RESEARCH ARTICLE | CELL BIOLOGY

# De novo mutations in KIF1A-associated neuronal disorder (KAND) dominant-negatively inhibit motor activity and axonal transport of synaptic vesicle precursors

Yuzu Anazawa[a,1], Tomoki Kita[b,1], Rei Iguchi[a], Kumiko Hayashi[b,c], and Shinsuke Niwa[a,d,2]

Edited by Ahmet Yildiz, University of California Berkeley Biophysics Group, Berkeley, CA; received July 27, 2021; accepted June 15, 2022 by Editorial Board Member Liqun Luo

**KIF1A is a kinesin superfamily motor protein that transports synaptic vesicle precursors in axons. Cargo binding stimulates the dimerization of KIF1A molecules to induce processive movement along microtubules. Mutations in human *Kif1a* lead to a group of neurodegenerative diseases called KIF1A-associated neuronal disorder (KAND). KAND mutations are mostly de novo and autosomal dominant; however, it is unknown if the function of wild-type KIF1A motors is inhibited by heterodimerization with mutated KIF1A. Here, we have established *Caenorhabditis elegans* models for KAND using CRISPR-Cas9 technology and analyzed the effects of human KIF1A mutation on axonal transport. In our *C. elegans* models, both heterozygotes and homozygotes exhibited reduced axonal transport. Suppressor screening using the disease model identified a mutation that recovers the motor activity of mutated human KIF1A. In addition, we developed in vitro assays to analyze the motility of heterodimeric motors composed of wild-type and mutant KIF1A. We find that mutant KIF1A significantly impaired the motility of heterodimeric motors. Our data provide insight into the molecular mechanism underlying the dominant nature of de novo KAND mutations.**

KIF1A | KAND | axonal transport | synaptic vesicles | kinesin

Neuronal function depends on an intricate intracellular transport system driven by motor proteins that move processively and directionally along microtubules (1). Kinesin superfamily proteins (KIFs) and cytoplasmic dynein are molecular motors for anterograde and retrograde transport, respectively (2, 3). Various membranous organelles and protein complexes are transported long distances by kinesin-1, -2, and -3 family members (4–8). Neurons transmit information via synaptic vesicles (9). The components of synaptic vesicles are synthesized in the cell body and subsequently transported to synapses along the axon (7). The transported organelle, called a synaptic vesicle precursor, is transported by kinesin superfamily protein 1A (KIF1A), a kinesin-3 family member (7, 10). KIF1A is composed of an N-terminal motor domain and a C-terminal cargo-binding tail domain (7). The motor domain, conserved among kinesin superfamily members, has microtubule-dependent ATPase activity that drives movement along microtubules (11, 12). The tail domain of KIF1A is composed of a protein-binding stalk domain and a lipid-binding Pleckstrin-homology (PH) domain (10, 13–15).

*Caenorhabditis elegans* provides a good model system to study axonal transport (16–23). UNC-104 is a *C. elegans* ortholog of KIF1A (6, 24). Electron and light microscopy analyses have shown that synapses, as well as synaptic vesicles, are mislocalized in *unc-104* loss-of-function mutants (6). The mechanism of axonal transport is well conserved between *C. elegans* and mammals and the expression of human *Kif1a* complementary DNA (cDNA) can rescue the phenotype of *unc-104* mutant worms (25).

In humans, mutations in the motor domain of KIF1A cause congenital neuropathies (26–28). More than 60 mutations have been found within the motor domain of KIF1A in neuropathy patients. Some cases are familial, but most are sporadic. For example, KIF1A(R11Q) was found in a spastic paraplegia patient who has autism spectrum disorder and attention-deficit hyperactivity disorder (29). The KIF1A(R254Q) mutation was found in Japanese spastic paraplegia patients with intellectual disability (30). KIF1A(R254) is a hot spot for mutations that result in a broad range of neuropathies (27). The range of neuropathies caused by KIF1A mutations are called KIF1A-associated neuronal disorder (KAND) (27). Both dominant and recessive mutations are associated with KAND. Recent in vitro studies have shown that many KAND mutations result in the loss of KIF1A motor function. KIF1A(V8M) causes defects in force generation, while KIF1A(R254W), KIF1A(A255V), and KIF1A(R350G) have a shorter run length (27, 31, 32). The KIF1A(P305L) mutation strongly reduces the microtubule

## Significance

KIF1A transports synaptic vesicle precursors in axons. Recent studies have identified many *KIF1A* mutations in congenital neuropathy patients; however, the molecular mechanism of pathogenesis remains largely elusive. This study established loss-of-function models for KIF1A-associated neuronal disorder (KAND) in *Caenorhabditis elegans* to analyze the molecular and cell biology of the disease in vivo. Genetic screening using the disease model identified a suppressor mutation that recovers the motor activity of mutated KIF1A. This study also established in vitro single-molecule assays to quantitatively analyze the effect of KAND mutations on heterodimeric motors composed of mutant and wild-type copies of KIF1A. Our findings provide a foundation for future genetic and drug screening in the effort to identify novel KAND therapies.

Author contributions: K.H. and S.N. designed research; Y.A., T.K., and S.N. performed research; Y.A., R.I., and S.N. contributed new reagents/analytic tools; Y.A., T.K., and S.N. analyzed data; and Y.A., T.K., K.H., and S.N. wrote the paper.

The authors declare no competing interest.

This article is a PNAS Direct Submission. A.Y. is a guest editor invited by the Editorial Board.



[1]Y.A. and T.K. contributed equally to this work.

[2]To whom correspondence may be addressed. Email: shinsuke.niwa.c8@tohoku.ac.jp.

This article contains supporting information online at http://www.pnas.org/lookup/suppl/doi:10.1073/pnas.2113795119/-/DCSupplemental.

Published August 2, 2022.

association rate of the motor, while KIF1A(R169T) disrupted the microtubule-dependent ATPase activity of the motor domain (33, 34). On the other hand, we have suggested that KIF1A(V8M), KIF1A(A255V), and KIF1A(R350G) mutations (all of them are familial) result in a gain of function (25). An in vitro analysis using the full-length human KIF1A as well as worm models established by CRISPR-Cas9 suggested that these mutations disrupt an autoinhibitory mechanism that inhibits KIF1A motor activity in the absence of cargo. These mutations result in overactive KIF1A, leading to an aberrant increase in the axonal transport of synaptic vesicle precursors.

While loss-of-function mutations have been intensively studied using in vitro assays, reliable models to study the neuronal cell biology of loss-of-function KAND mutations in vivo are lacking. Moreover, previous in vitro studies have mostly analyzed homodimers composed of disease-associated KIF1A (27, 33) because it was difficult to purify heterodimers composed of wild-type and disease-associated KIF1A (31). Activated KIF1A forms a homodimer in order to move along microtubules (35), and it is thus likely that wild-type KIF1A (KIF1A(wt)) motors will dimerize with disease-associated KIF1A in patient neurons. However, the properties of heterodimers composed of KIF1A(wt) and disease-associated KIF1A remain unknown, and it is unclear whether de novo KAND mutations inhibit the function of KIF1A(wt) in a dominant-negative fashion.

Here, we established models of de novo KAND mutations in the nematode *C. elegans*. Both heterozygous and homozygous worms show synaptic deficiencies that are caused by defects in axonal transport. Unbiased suppressor screening using the worm model identified a mutation that recovers the motor activity of disease-associated human KIF1A. We also established an in vitro single-molecule assay to measure the motility parameters of a single KIF1A heterodimer composed of wild-type and mutant motors. Both our in vitro and in vivo analysis suggest a dominant-negative nature of disease-associated mutations in humans.

## Results

***C. elegans* Models of De Novo KAND.** To study molecular and cellular deficiencies caused by de novo disease-associated KIF1A mutations, we established *C. elegans* models for KAND using CRISPR-Cas9 (36). The *C. elegans unc-104* gene is an ortholog of human *Kif1a*, and the human gene can rescue defects caused by knockout of *unc-104*, suggesting the human and worm genes are highly similar in structure and function. We introduced the following mutations into the *unc-104* gene: *unc-104(R9Q)*, *unc-104(R251Q)*, and *unc-104(P298L)* (Fig. 1 *A* and *B* and *SI Appendix*, Fig. S1*A*). These UNC-104 residues are conserved in human KIF1A, and the mutations we introduced correspond to KIF1A(R11Q), KIF1A(R254Q), and KIF1A(P305L) mutations that cause de novo and autosomal dominant KAND, respectively (29, 30, 33). Introduction of the mutations was confirmed by digestion with restriction enzymes and Sanger sequencing (*SI Appendix*, Fig. S1*A*). We then observed the macroscopic phenotypes of disease model homozygous worms. As a control, a strong loss-of-function allele of *unc-104*, *unc-104(e1265)* (hereafter referred to as *unc-104(lf)*), was included. Homozygous worms showed strong uncoordinated (unc) phenotypes and did not move well on the culture plate (Fig. 1C). To quantitively analyze the movement of worms, the number of body bends in a water drop was counted (*SI Appendix*, Fig. S1*B*). We found that *unc-104(R9Q)*, *unc-104(R251Q)*, and *unc-104(P298L)* showed a similar defect in body bending as *unc-104(lf)*. Moreover, the body size of homozygous worms was smaller than *wild type* (1.09 ± 0.09 mm, 0.66 ± 0.06 mm, 0.64 ± 0.07 mm, 0.74 ± 0.06 mm, and 0.81 ± 0.14 mm, mean ± SD in length, respectively, in *wild type*, *unc-104(R9Q)*, *unc-104(R251Q)*, *unc-104(P298L)*, and *unc-104(lf)*) (Fig. 1*C* and *SI Appendix*, Fig. S1*C*). These results collectively show that the KIF1A(R11Q), KIF1A(R254Q), and KIF1A(P305L) mutations likely result in loss of motor function, as we observe here for the homologous mutations introduced into *unc-104*.

**Synaptic Vesicles Are Mislocalized in Homozygotes.** UNC-104 is a molecular motor that determines the localization of synaptic vesicles in *C. elegans*, and we therefore visualized the localization of synaptic vesicles in our KAND model worms. The DA9 neuron in *C. elegans* is highly polarized and forms *en passant* synapses along the dorsal side of the axon (37) (Fig. 2*A*). The characteristic morphology of the DA9 neuron is suitable for analyzing axonal transport and synaptic localization (38).

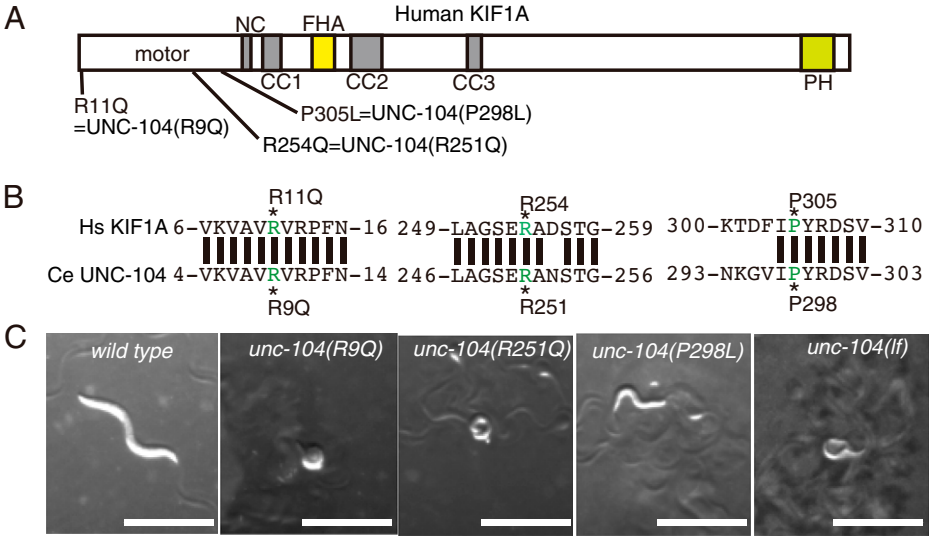


**Fig. 1.** (*A*) Schematic drawing of the domain organization of KIF1A motor protein. NC, neck coiled-coil domain. CC1, Coiled-coil 1 domain. FHA, Forkhead-associated domain. CC2, Coiled-coil 2 domain. CC3, Coiled-coil 3 domain. The three KAND mutations and corresponding *C. elegans* UNC-104 mutations analyzed in this study are indicated. (*B*) Sequence comparison between human KIF1A and *C. elegans* UNC-104. (*C*) Macroscopic phenotypes of KAND model homozygotes at 1-d adults. Mutant worms are smaller than *wild-type* worms and do not move well on the bacterial feeder. Bars, 1 mm. See also *SI Appendix*, Fig. S1.

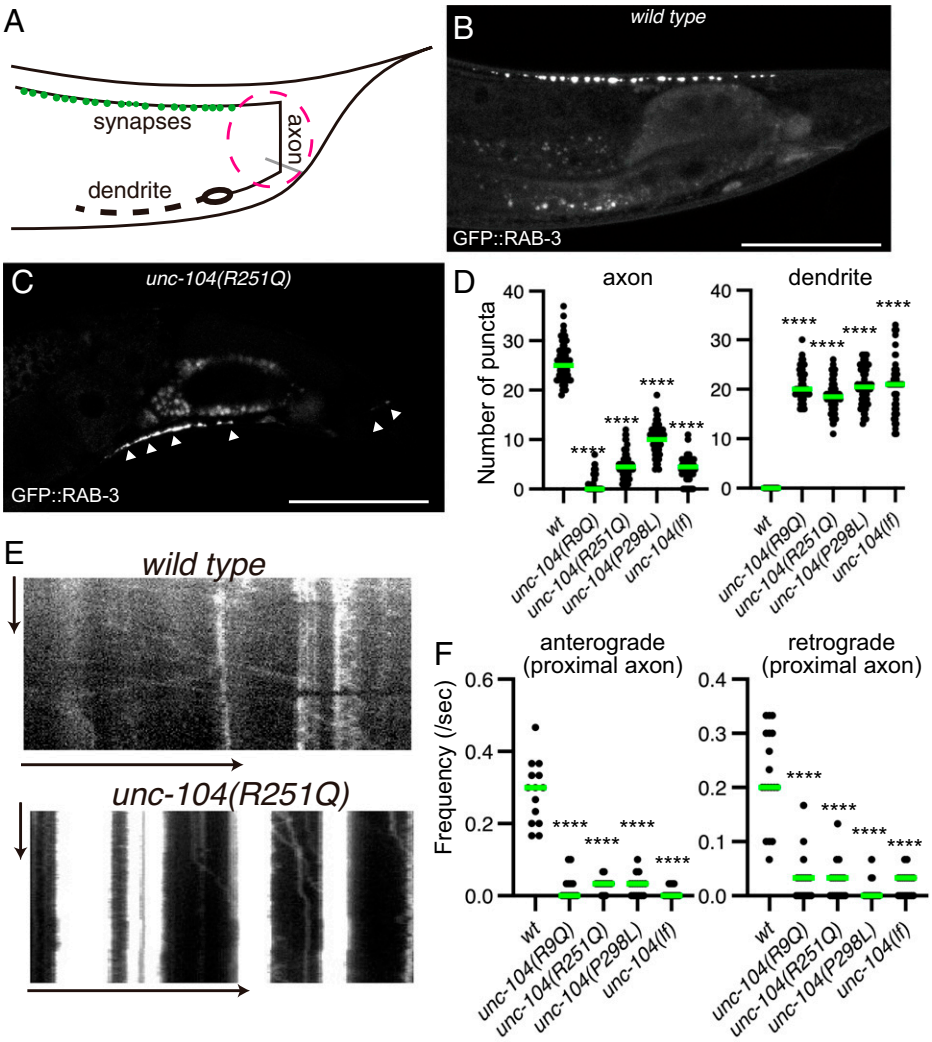


**Fig. 2.** Synaptic vesicle localization in KAND model homozygote worms. (*A*) Schematic drawing shows the morphology of the DA9 neuron. Green dots along the axon show synaptic vesicle distribution. The red circle shows proximal axon. (*B* and *C*) Representative images showing the distribution of synaptic vesicles in the DA9 neuron in *wild type* (*B*) and *unc-104(R251Q)* (*C*). Synaptic vesicles are visualized by GFP::RAB-3. Arrowheads show mislocalization of synaptic vesicles in the dendrite and proximal axon. Bars, 50 μm. (*D*) Dot plots showing the number of puncta in the dorsal axon (*Left* panel) and ventral dendrite (*Right* panel) of DA9. Green bars represent median value. Kruskal–Wallis test followed by Dunn's multiple comparison test. $n = 60$ worms for each genotype. ****, Adjusted *P* value of <0.0001. (*E*) Representative kymographs in *wild type* (*Upper* panel) and *unc-104(R251Q)* (*Lower* panel). The axonal transport of synaptic vesicle precursors was visualized by GFP::RAB-3. The proximal axon shown in *A* was observed. Vertical and horizontal arrows show 10 s and 10 μm, respectively. (*F*) Dot plots showing the frequency of anterograde axonal transport (*Left* panel) and retrograde axonal transport (*Right* panel). Green bars represent median value. Kruskal–Wallis test followed by Dunn's multiple comparison test. $n = 14$ *wild type*, 14 *unc-104(R9Q)*, 18 *unc-104(R251Q)*, 16 *unc-104(P298L), and 18 unc-104(lf)* axons. ****, Adjusted *P* value of <0.0001. See also *SI Appendix*, Fig. S2.

We expressed the synaptic vesicle marker GFP::RAB-3 in the DA9 neuron using the *itr-1* promoter to visualize DA9 synapses (Fig. 2*B*). In KAND models, GFP::RAB-3 signals were reduced in the axon and strongly mislocalized within the dendrite (Fig. 2 *C* and *D* and *SI Appendix*, Fig. S2). Only a trace amount of the GFP::RAB-3 signal was observed in the DA9 axon in KAND models.

*We* then observed axonal transport of synaptic vesicle precursors in the proximal region of the DA9 axon (38) (Fig. 2*A*, magenta circle). We used GFP::RAB-3 as a representative marker for axonal transport of synaptic vesicle precursors because previous studies have shown that GFP::RAB-3 comigrates with other synaptic vesicle and presynaptic proteins in the axon (10, 23, 38) and that RAB3A, a mammalian ortholog of RAB-3, comigrates with KIF1A in mouse neurons (10). In the *wild type* worms, both anterograde and retrograde transport were observed in the axon (Fig. 2 *E* and *F*). In contrast, the frequency of both anterograde and retrograde events was significantly reduced in all three mutant strains (Fig. 2 *E* and *F*). In more than 70% of the mutant worms, no vesicular movement was detected in the 30-s time window. Similar phenotypes are observed in the loss-of-function allele of *unc-104*. These data indicate that the axonal transport of synaptic vesicles is strongly reduced in *unc-104(R9Q)*, *unc-104(R251Q)*, and *unc-104(P298L)* strains, consistent with the idea that these mutations result in the loss of *unc-104* motor function.

**KAND Mutations Disrupt the Motility of Motor Proteins In Vitro.** To study the effect of KAND mutations in vitro, we analyzed the motility of purified human KIF1A protein using total internal reflection fluorescence (TIRF) microscopy (39, 40). To directly study the motility parameters of the motors, the C-terminal regulatory and cargo binding domains were removed (Fig. 3*A*). The neck coiled-coil domain of mammalian KIF1A does not form stable dimers without cargo binding (41), and we therefore stabilized human KIF1A dimers

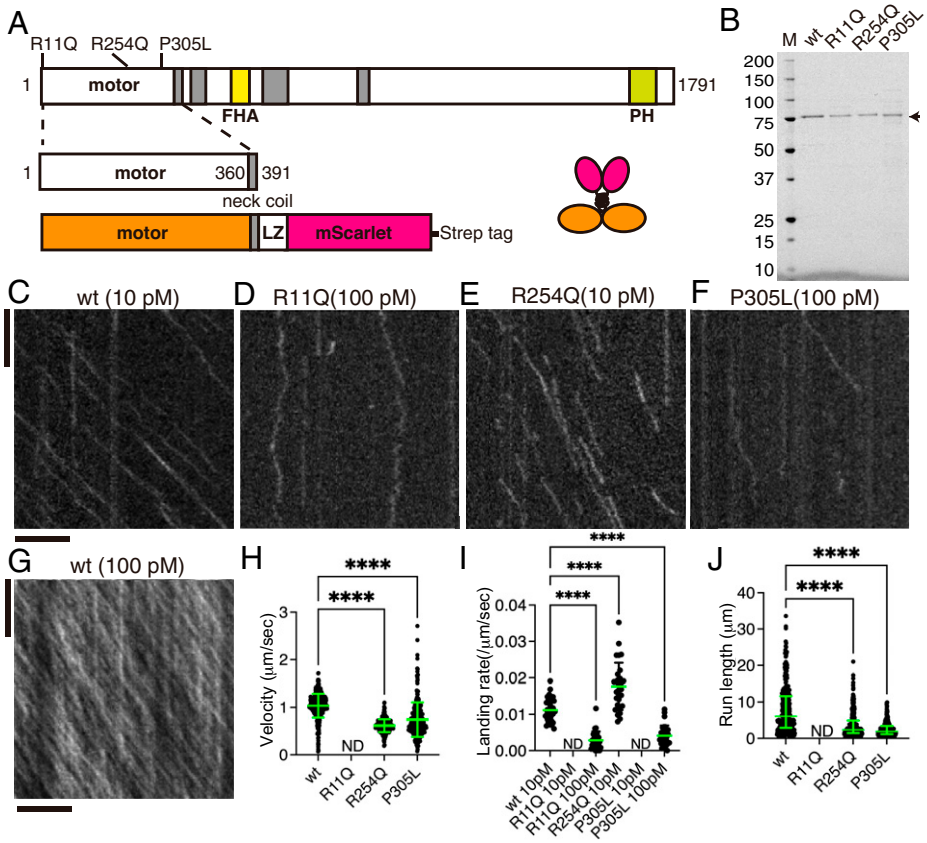


**Fig. 3.** Single-molecule behavior of disease-associated KIF1A mutants. (*A*) Schematic drawing of the domain organization of KIF1A motor protein and recombinant protein analyzed in Fig. 3. (*B*) Purified KIF1A(1–393)::LZ::mScarlet and its mutants were separated by sodium dodecyl-sulfate polyacrylamide gel electrophoresis (SDS-PAGE) and detected by trichloroethanol staining. M represents a marker lane. Numbers on the left indicate molecular weight (kDa). Arrow indicates KIF1A(1–393)::LZ::mScarlet. (*C*–*G*) Representative kymographs showing the motility of 10 pM KIF1A(wt) (*C*), 100 pM KIF1A(R11Q) (*D*), 10 pM KIF1A(R254Q) (*E*), 100 pM KIF1A(P305L), and 100 pM KIF1A(wt) (*G*). Vertical and horizontal bars represent 5 s and 5 μm, respectively. (*H*) Dot plots showing the velocity of KIF1A. Each dot indicates one datum. Green bars represent mean ± SD. Kruskal–Wallis test followed by Dunn's multiple-comparison test. $n$ = 433 (wt), 325 (R254Q), and 498 (P305L). ****, Adjusted $P$ value of <0.0001. Note that no processive movement was detected for KIF1A(R11Q). ND, not detected. (*I*) Dot plots showing the landing rate of KIF1A. The number of KIF1A that bound to microtubules was counted and adjusted by the time window and microtubule length. Each dot shows one datum. Green bars represent median value. Kruskal–Wallis test followed by Dunn's multiple comparison test. $n$ = 30 (10 pM wt), 28 (100 pM R11Q), 29 (10 pM R254Q), and 30 (100 pM P305L) movies. ****, Adjusted $P$ value of <0.0001. Compared with KIF1A(wt). Note that no landing event was detected in 10 pM KIF1A(R11Q) and KIF1A(P305L) experiments. (*J*) Dot plots showing the run length of KIF1A. Each dot shows one datum. Green bars represent median value and interquartile range. Kruskal–Wallis test followed by Dunn's multiple comparison test. $n$ = 312 (wt), 241 (R254Q), and 243 (P305L) homodimers. ****, Adjusted $P$ value of <0.0001. Note that all KIF1A motility events were included, including those that end when the motor reaches the end of a microtubule; thus, the reported run lengths are an underestimation of the motor's processivity. See also *SI Appendix*, Fig. S3.

using a leucine zipper domain as described previously (27, 33). A red fluorescent protein, mScarlet-I, was added to the C terminus of the protein to observe the movement (Fig. 3*A*). Resultant KIF1A homodimers [KIF1A(1-393)::LZ::mSca] were purified by Strep tag and gel filtration (Fig. 3*B* and *SI Appendix*, Fig. S3*A*). All the recombinant proteins were recovered from the same fractions in the gel filtration. The recombinant protein was then used to analyze the motility of single KIF1A dimers on microtubules (Fig. 3 *C*–*J*). We observed robust processive motility of KIF1A(1-393)::LZ::mSca dimers at a 10 pM motor concentration (Fig. 3*C*). KIF1A(1-393)(R11Q)::LZ::mSca did not move at all on microtubules even at 100 pM (Fig. 3*D*), while KIF1A(1-393)::LZ::mSca was saturated on microtubules under the same condition (Fig. 3*G*). KIF1A(1–393)(R11Q)::LZ::mSca showed only one-dimensional Brownian motion on microtubules, while KIF1A(1-393)(R254Q)::LZ::mSca showed processive movement on microtubules at 10 pM (Fig. 3*E*). While we observed a higher binding frequency of KIF1A(1-393)(R254Q)::LZ::mSca as compared to KIF1A(wt) (Fig. 3*I*), the average velocity was 50% lower and the average run length was 70% shorter (Fig. 3 *H* and *J*). The landing rate and run length of KIF1A(1–393)(P305L)::LZ::mSca were significantly lower than KIF1A(wt) (Fig. 3*I*), consistent with previous studies (27, 33). Although the affected biophysical parameters were different depending on the mutated residues, these data are consistent with the reduced axonal transport phenotypes observed in KAND model worms and reveal that specific mutations affect distinct biophysical outputs of the mutant motors.

In contrast to the well-characterized KIF1A(P305L) mutation (33), properties of KIF1A(R11Q) and KIF1A(R254Q) mutations have not been analyzed thoroughly. We compared the binding of these two mutants with microtubules in the presence of ADP and an AMP-PNP (an ATP analog) (*SI Appendix*, Fig. S3 *B*–*E*). The binding of KIF1A(R254Q) with microtubules is comparable to KIF1A(wt) in the presence of AMP-PNP but much weaker and more unstable in the presence of ADP (*SI Appendix*, Fig. S3 *B*–*D*). KIF1A(1-393)(R11Q)::LZ::mSca did not stably bind to microtubules even in the presence of AMP-PNP (*SI Appendix*, Fig. S3 *D* and *E*). These results suggest that R11Q and R254Q affect microtubule binding by different mechanisms, which can account for the different property of these two mutant proteins (*Discussion*).

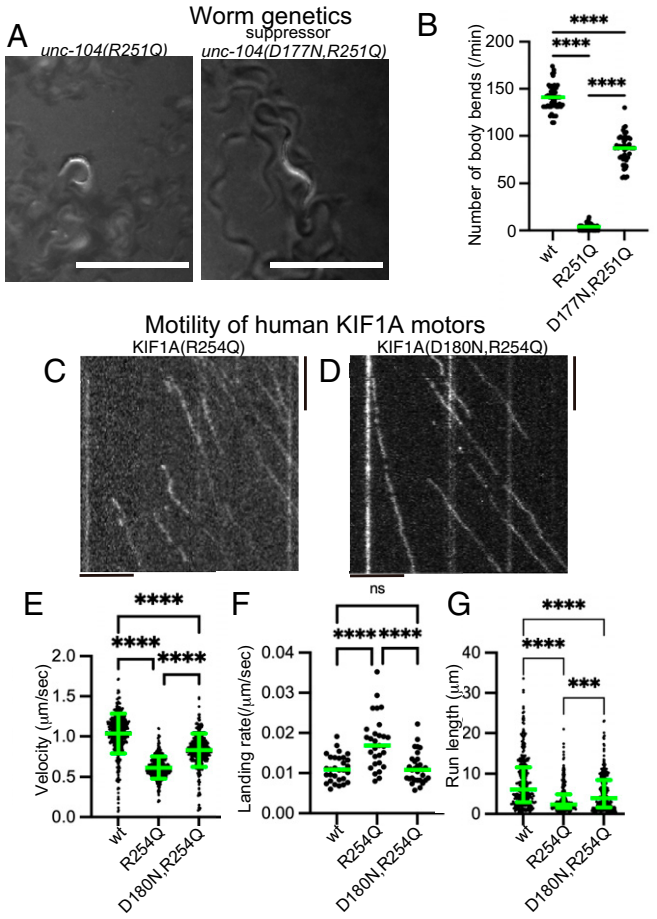


**Fig. 4.** Suppressor screening. (*A*) Macroscopic phenotypes of *unc-104(R251Q)* and a suppressor mutant *unc-104(D177N, R251Q).* While *unc-104(R251Q)* worms do not move well on the bacterial feeder, *unc-104(D177N, R251Q)* worms move smoothly. Bars, 1 mm. (*B*) Dot plots showing the result of swim test. The number of body bends in a water drop was counted for 1 min and plotted. Dots represents the number of bends from each worm. Green bars represent median value. Kruskal–Wallis test followed by Dunn's multiple comparison test. $n$ = 20 worms for each genotype. ****, Adjusted $P$ value of <0.0001. (*C* and *D*) Representative kymographs showing the motility of 10 pM human KIF1A(R254Q) protein (*C*) and KIF1A(D180N, R254Q) protein (*D*) on microtubules. Vertical and horizontal bars represent 5 s and 5 μm, respectively. (*E*) Dot plots showing the velocity of KIF1A. Dot shows the actual value from each data point. Green bars represent mean ± SD. Kruskal–Wallis test followed by Dunn's multiple comparison test. $n$ = 433 (wt), 325 (R254Q), and 368 (D180N, R254Q). ****, Adjusted $P$ value of <0.0001. (*F*) Dot plots showing the landing rate of KIF1A. The number of KIF1A that bound to microtubules was counted and adjusted by the time window and microtubule length. Green bars represent median value. Kruskal–-Wallis test followed by Dunn's multiple comparison test. $n$ = 30 (10 pM wt), 29 (10 pM R254Q), and 30 (10 pM D180N, R254Q). ****, Adjusted $P$ value of <0.0001. (*G*) Dot plots showing the run length of KIF1A. Green bars represent median value and interquartile range. Kruskal–Wallis test followed by Dunn's multiple comparison test. $n$ = 312 (wt), 241 (R254Q), and 312 (D180N, R254Q) homodimers. ****, Adjusted $P$ value of <0.0001. Note that the reported run lengths are an underestimation of the motor's processivity. as described in Fig. 3*J* and that KIF1A(wt) and KIF1A(R254Q) values are the same with Fig. 3. See also *SI Appendix*, Fig. S4.

**Genetic Screening in KAND Model Worm Identified a Mutation That Recovers the Motility of Mutant KIF1A.** To show the advantage of the disease model worm, we performed a genetic screening and searched for mutants that recover the body movement of *unc-104(R251Q)* model worms (Fig. 4*A*). From about 10,000 haploid genomes, we recovered 2 independent suppressors. Interestingly, genomic sequencing revealed that these two independent suppressor lines have the same mutation, UNC-104(D177N). While *unc-104(R251Q)* worms did not move well, *unc-104(D177N,R251Q)* worms showed much better performance in the swimming assay (Fig. 4*B*). *unc-104(D177N, R251Q)* worms had clear synaptic puncta in the dorsal synaptic region, while a very small number of dorsal synaptic puncta were observed in *unc-104(R251Q)* worms (*SI Appendix*, Fig. S4 *A–D*). D177 in *C. elegans* UNC-104 is equivalent to D180 in human KIF1A, a residue located in the β5 region of the motor domain. We then compared the activity of the human KIF1A(R254Q) protein and KIF1A(D180N,R254Q) protein in our in vitro single-molecule assays (Fig. 4 *C–G*). We found that the three motility parameters altered in KIF1A(R254Q) were largely recovered by the additional KIF1A(D180N) mutation (Fig. 4 *E–G*), consistent with the rescued worm phenotypes described above. These data suggest phenotypes of our KAND model worms can be utilized to screen for suppressor mutations relevant to the activity of the human KIF1A motor.

**Synaptic Vesicles Are Mislocalized in Heterozygous Worms.** KAND mutations, including KIF1A(R11Q), KIF1A(R254Q), and KIF1A(P305L) studied here, are de novo and cause neuropathies in an autosomal dominant manner. Moreover, KAND is a progressive disease. We therefore analyzed neuronal phenotypes of heterozygous worms in late adult stages (Fig. 5 *A–F*). RT-PCR followed by restriction enzyme digestion confirmed that the expression level of *wild-type* and mutant *unc-104* messenger RNA was highly similar (*SI Appendix*, Figs. S1*A* and S5*A* and *Methods*). We included a null allele of *unc-104*, *unc-104(tm819)*, as a control. This allele contains a large deletion mutation in the motor-domain coding region. *unc-104(tm819)* homozygotes were lethal but heterozygotes were viable, and we thus described the allele as *unc-104(null)* for the rest of this paper. DA9 synapses and body movement in water were analyzed in heterozygotes at 1 d, 3 d, 6 d, and 9 d after the final molt (Fig. 5 *A–F* and *SI Appendix*, Fig. S5 *B–I*). No significant differences were observed at 1-d adults (*SI Appendix*, Fig. S5 *B–D*). At day 3, some disease-associated heterozygotes showed mislocalization of synaptic vesicles in the dendrite (Fig. 5 *A* and *B* and *SI Appendix*, Fig. S5 *E–G*). At day 6 and 9, dendritic mislocalization was clearly observed in 45 to 70% *unc-104(R9Q)*/+, *unc-104(R251Q)*/+, and u*nc-104(P298L)*/+ worms (Fig. 5 *C–E*). In contrast, the mislocalization of synaptic puncta in *unc-104(null)*/+ was comparable to *wild-type* controls in all age adults (Fig. 5*E* and *SI Appendix*, Fig. S5 *C* and *F*). In contrast to the KAND alleles, more than 70% of *wild-type* and *unc-104(null)*/+ worms showed normal distribution of GFP::RAB-3 in the dendrite, even at 6 and 9 d (Fig. 5*E*). The number of dorsal axonal puncta were not significantly affected in all age adults in all genotypes (*SI Appendix*, Fig. S5 *B*, *E*, *H*, and *I*). Similar to the dendritic mislocalization phenotypes, worm movement was slightly affected by 6 or 9-d in *unc-104(R9Q)*/+, *unc-104(R251Q)*/+, and u*nc-104(P298L)*/+ adults (Fig. 5*F*). The defect is more evident at day 9. In contrast, the body movement of unc-*104(null)*/+ was comparable to age-matched *wild-type* worms (Fig. 5*F*). Overall, the phenotypes of *unc-104(R9Q)*/+, *unc-104(R251Q)*/+, and *unc-104(P298L)*/+ were stronger than *unc-104(null)*/+, suggesting that the KAND mutations result in dominant-negative phenotypes for *unc-104* transport in living animals.

**Reduced Axonal Transport in KAND Heterozygote Worms.** The DA9 axon and dendrite contain plus-end out and minus-end out microtubules, respectively (42). We analyzed axonal and dendritic transport on day 1 after the final molting to exclude the possibility that a disrupted neuronal morphology could indirectly alter cargo transport parameters. In *wild-type*, *unc-104(R9Q)*/+, *unc-104(R251Q)*/+, *unc-104(P298L)*/+, and *unc-104(null)*/+

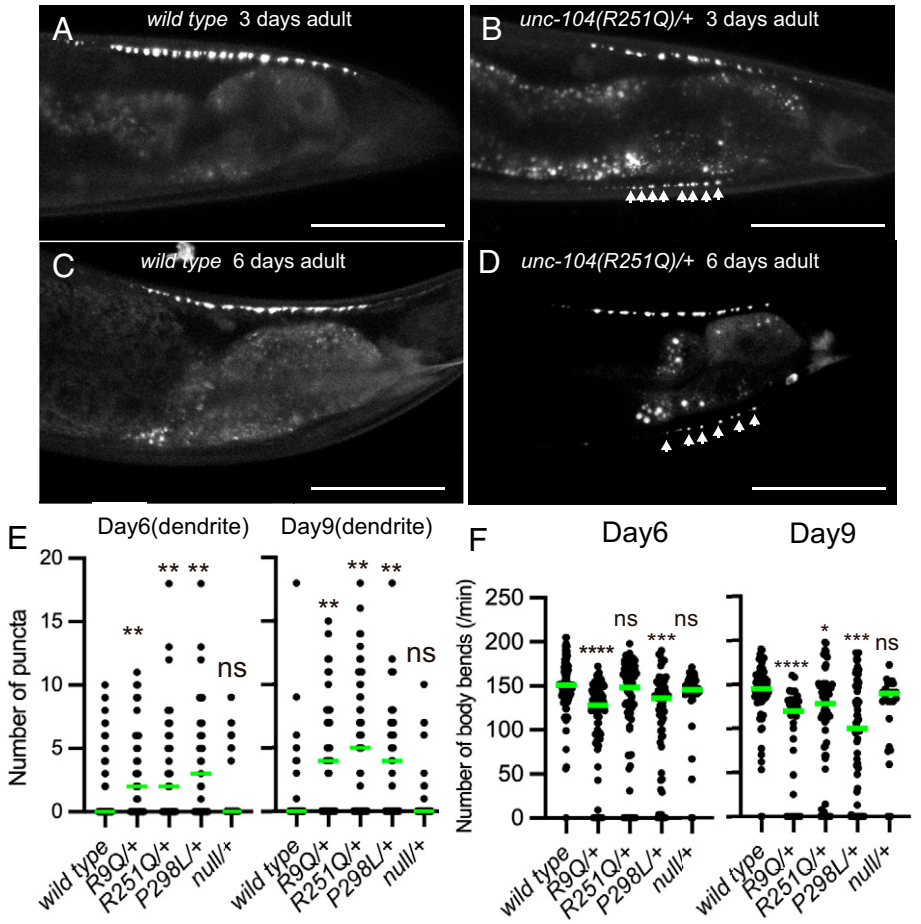


**Fig. 5.** Synaptic vesicle localization of heterozygotes. (*A–D*) Representative images showing synaptic vesicle distribution in 3-d *wild-type* adult (*A*), 3-d *unc-104(R251Q)/+* adult (*B*), 6-d *wild-type* adult (*C*), and 6-d *unc-104(R251Q)/+* adult (*D*). Synaptic vesicles are visualized by GFP::RAB-3. Arrowheads show mislocalization of synaptic vesicles in the dendrite. Bars, 50 μm. (*E*) Dot plots showing the number of dendritic puncta at 6 and 9 d. Each dot shows the number of puncta in the dendrite in each worm. Green bars represent median value. Kruskal–Wallis test followed by Dunn's multiple comparison test. $n$ = 59 (wt), 36 (R9Q/+), 46 (R251Q/+), 39 (P298L/+), and 40 (null/+) (6-d adult worms); 58 (wt), 38 (R9Q/+), 49 (R251Q/+), 40 (P298L/+), and 43 (null/+) (9-d adult worms). ns, adjusted $P$ value of >0.05 and statistically not significant. **, Adjusted $P$ value of <0.01. (*F*) Dot plots showing the result of swim test at 6 and 9 d. Each dot shows the number of bends in each measurement. Green bars represent median value. Kruskal–Wallis test followed by Dunn's multiple comparison test. $n$ = 76 (wt), 87 (R9Q/+), 74 (R251Q/+), 65 (P298L/+), and 38 (null/+) (6-d adult worms); 66 (wt), 30 (R9Q/+), 65 (R251Q/+), 67 (P298L/+), and 27 (null/+) (9-d adult worms). ns, adjusted $P$ value of >0.05 and statistically not significant. *, Adjusted $P$ value of <0.05. **, Adjusted $P$ value of <0.01. ****, Adjusted $P$ value of <0.0001. See also *SI Appendix*, Fig. S5.

worms, both anterograde and retrograde movement of synaptic vesicle precursors were observed in the proximal region of the DA9 axon (Figs. 2*A* and 6 *A–E*). Much more vesicular movement was observed in heterozygous than in homozygous worms (Fig. 2). However, in three disease-associated mutant heterozygotes, the velocity of anterograde axonal transport was reduced (Fig. 6*B*). No significant difference in anterograde velocity was detected in *unc-104(null)/+* worms. In contrast, retrograde velocity, which depends on the cytoplasmic dynein motor, was not significantly changed in all mutant heterozygotes (Fig. 6*C*). The frequency of both anterograde and retrograde axonal transport was reduced in KAND mutant heterozygotes (Fig. 6 *D* and *E*). The directionality of vesicular transport was not significantly changed in KAND mutants (Fig. 6*F*). These results are consistent with previous studies showing the codependence of anterograde and retrograde motor machineries on bidirectional vesicular trafficking (38, 43–45). In the DA9 dendrite, even though the accumulation of immotile puncta was not observed in *wild type* (Fig. 2 *A* and *B*), some motile vesicles could be detected as previously described (37). While the velocity of retrograde transport (i.e., transport from the dendritic tip to the cell body) was slightly reduced, other parameters, such as frequency of movement, were not strongly affected (*SI Appendix*, Fig. S6 *A–E*). This may be because multiple classes of microtubule motors transport synaptic vesicle precursors within the dendrite (38). These data are consistent with a previous mathematical model showing that misaccumulation of synaptic vesicles to the dendrite is caused mainly by reduced anterograde transport in the proximal axon (38).

**KAND Heterodimer Motors Have Reduced Motor Properties.** The KIF1A motor forms a homodimer for efficient anterograde axonal transport (35). In patients who have autosomal dominant mutations, half of the motor complex in the neuron is expected to be heterodimers composed of wild-type and disease-associated copies of the KIF1A protein. But the behavior of heterodimers on microtubules remains largely unanalyzed. We therefore purified heterodimers composed of one wild-type and one disease-associated subunit of KIF1A. KIF1A(wt) fused with leucine zipper and mScarlet-I (KIF1A(1-393)::LZ::mSca) and disease-associated KIF1A without fluorescent tag (KIF1A(1-393)::LZ) were coexpressed in bacteria (Fig. 7*A*). The two constructs were respectively fused with Strep and His tags for sequential purification. Tandem affinity purification using His tag and Strep tag followed by gel filtration was performed to purify the motor heterodimers. These heterodimers were recovered from the same peak fractions (Fig. 7*B* and *SI Appendix*, Fig. S7), where

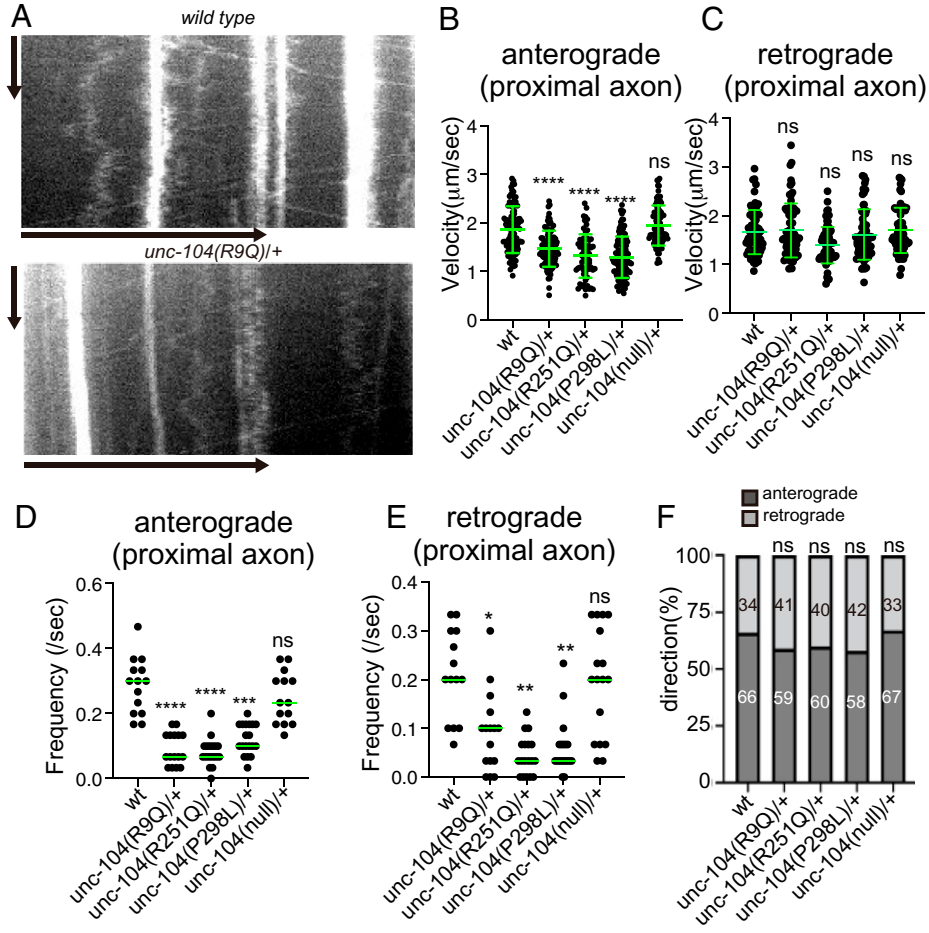


**Fig. 6.** Axonal transport in KAND model heterozygotes (*A*) Representative kymographs showing axonal transport of synaptic vesicle precursors in *wild type* and *unc-104(R9Q)/+* at 1 d adults. GFP::RAB-3 was used as a marker. Vertical and horizontal bars show 10 s and 10 μm, respectively. (*B* and *C*) The velocity of axonal transport. The velocity of anterograde transport (*B*) and retrograde transport (*C*) are shown as dot plots. (*B*) Kruskal–Wallis test followed by Dunn's multiple comparison test. Green bars show mean ± SD $n = 94$ (*wild type*), 90 (R9Q/+), 66 (R251Q/+), 117 (P298L/+) and 84 (null/+) vesicles from at least 5 independent worms. ns, Adjusted $P$ value > 0.05 and no significant statistical difference. ****, Adjusted $P$ value < 0.0001. (*C*) Kruskal-Wallis test followed by Dunn's multiple comparison test. Green bars show mean ± SD; $n = 70$ (*wild type*), 70 (R9Q/+), 68 (R251Q/+), 63 (P298L/+), and 65 (null/+) vesicles from at least 5 independent worms. ns, adjusted $P$ value of >0.05 and no significant statistical difference. (*D* and *E*) Frequency of axonal transport. The frequency of anterograde transport (*D*) and retrograde transport (*E*) are shown as dot plots. (*E*) Kruskal–Wallis test followed by Dunn's multiple comparison test. Each dot represent data from each worm. Green bars represent median value. $n = 14$ (wt), 16 (R9Q/+), 18 (R251Q/+), and 19 (P298L/+) independent worms. ****, Adjusted $P$ value of <0.0001. (*E*) Kruskal–Wallis test followed by Dunn's multiple comparison test. Each dot represent data from each worm. Green bars represent median value. $n = 14$ (wt), 16 (R9Q/+), 18 (R251Q/+), and 19 (P298L/+) independent worms. **, Adjusted $P$ value of <0.01; ****, Adjusted $P$ value of <0.0001. (*F*) Directionality of vesicle movement. The number in the bar graph shows the actual percentage. ns, Adjusted $P$ value of >0.05 and statistically not significant. $\chi^2$ test. Compared to wt worms. See also *SI Appendix*, Fig. S6.

the ratio between two subunits calculated from band intensities and molecular weight was about 1:1.

As a positive control, we compared the motility of heterodimers composed of KIF1A(1-393)::LZ::mSca and KIF1A(1-393)::LZ with KIF1A(1-393)::LZ::mSca homodimers (Figs. 3*C* and 7*C*). Velocity, landing rate, and run length of wild-type homodimers and heterodimers were statistically the same (velocity: 1.03 ± 0.24 μm/sec and 1.03 ± 0.26 μm/sec, run length: 7.99 ± 6.42 μm and 8.07 ± 6.30 μm, landing rate: 0.011 ± 0.003 μm $^{-1}$s$^{-1}$ and 0.010 ± 0.004 μm $^{-1}$s$^{-1}$ for homodimers and heterodimers, respectively. Mean ± SD. No significant differences by $t$ test.). In contrast, heterodimers composed of wild-type motor and KAND motor showed reduced motility (Fig. 7 *C–J*). Surprisingly, even though homodimers of KIF1A(1–393)(R11Q)::LZ::mSca showed no processive movement on microtubules, heterodimers composed of KIF1A(1–393)::LZ::mSca and KIF1A(1–393)(R11Q)::LZ (KIF1A(1-393)$^{wt/R11Q}$::LZ::mSca) did move processively (Fig. 7*D*). In addition, the other two heterodimers analyzed also showed processive movement (Fig. 7 *E* and *F*). The velocity of KIF1A (1-393)$^{wt/R11Q}$::LZ::mSca, KIF1A(1–393)$^{wt/R254Q}$::LZ::mSca, and KIF1A(1–393)$^{wt/P305L}$::LZ::mSca heterodimers was lower than that of KIF1A(1-393)$^{wt/wt}$::LZ::mSca (Fig. 7*H*). In contrast to wild type motors, the landing frequency of KIF1A(1–393)$^{wt/R11Q}$::LZ::mSca and KIF1A(1–393)$^{wt/P305L}$::LZ::mSca heterodimers on microtubules was below the limit of detection at 10 pM (Fig. 7*I*). At 100 pM, in which KIF1A(wt) homodimers were saturated on microtubules (Fig. 7*G*), the motility of KIF1A(1–393)$^{wt/R11Q}$::LZ::mSca and KIF1A(1–393)$^{wt/P305L}$::LZ::mSca heterodimers was observed (Fig. 7 *D*, *F*, and *I*), but the run lengths of these heterodimers were much shorter compared with that of wild-type dimers (Fig. 7*J*). The landing rate of KIF1A(1–393)$^{wt/R254Q}$::LZ::mSca heterodimers was slightly higher than that of wild-type dimers (Fig. 7*I*). However, the run length of KIF1A(1–393)$^{wt/R254Q}$::LZ::mSca heterodimers was shorter than that of wild-type dimers (Fig. 7*J*). These results show that KAND mutations strongly affect the landing rate and motility parameters of heterodimers formed with KIF1A(wt) and provide a molecular basis for the dominant phenotypes observed in these mutants in both humans and worms.

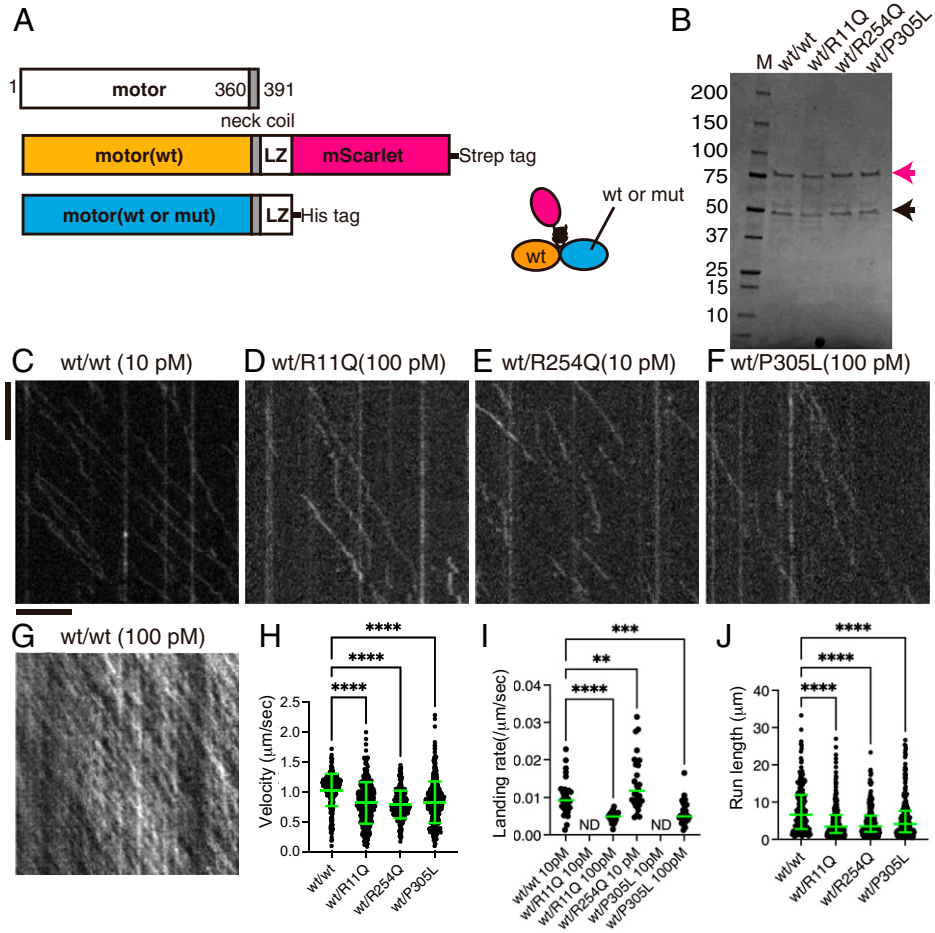


**Fig. 7.** The single-molecule behavior of wild-type/mutant KIF1A heterodimers. (*A*) Schematic drawing of the recombinant KIF1A heterodimer analyzed. (*B*) Purified KIF1A(1–393)::LZ::mScarlet/KIF1A(1–393)::LZ heterodimers were separated by SDS-PAGE and detected by Coomassie brilliant blue staining. M represents marker. Numbers on the left indicate the molecular weight (kDa). Magenta and black arrows indicate KIF1A(1–393)::LZ::mScarlet and KIF1A(1–393)::LZ, respectively. (*C*–*G*) Representative kymographs showing the motility of 10 pM KIF1A (wt) (*C*), 100 pM KIF1A(R11Q) (*D*), 10 pM KIF1A(R254Q) (*E*), 100 pM KIF1A(P305L) (F), and 100 pM KIF1A (wt) (*G*). Vertical and horizontal bars represent 5 s and 5 μm, respectively. (*H*) Dot plots showing the velocity of KIF1A. Each dot shows a single datum point. Green bars represent mean ± SD. Kruskal–Wallis test followed by Dunn's multiple comparison test. $n$ = 308 (wt/wt), 315 (wt/R11Q), 294 (wt/R254Q), and 414 (wt/P305L) heterodimers. ****, Adjusted $P$ value of <0.0001. (*I*) Dot plots showing the landing rate of KIF1A. The number of KIF1A that binds to microtubules was counted and adjusted by the time window and microtubule length. Each dot shows a single datum point. Green bars represent median value. Kruskal–Wallis test followed by Dunn's multiple comparison test. $n$ = 29 (10 pM wt/wt), 29 (100 pM wt/R11Q), 28 (10 pM wt/R254Q),and 38 (100 pM wt/P305L) independent observations. **, Adjusted $P$ value of <0.01; ***, adjusted $P$ value of <0.001; ****, adjusted $P$ value of <0.0001. (*J*) Dot plots showing the run length of KIF1A. Each dot shows a single datum point. Green bars represent median value and interquartile range. Kruskal–Wallis test followed by Dunn's multiple comparison test. $n$ = 215 (wt/wt), 241 (wt/R11Q), 195 (wt/R254Q), and 266 (wt/P305L) heterodimers. ****, Adjusted $P$ value of <0.0001. Note that the reported run lengths are an underestimation of the motor's processivity as described in Fig. 3*J*. See also *SI Appendix*, Fig. S7.

**Dominant-Negative Effects of Disease-Associated Mutations In Vitro and In Vivo.** Multiple kinesin dimers cooperatively transport cargo vesicles in the cell (31, 46–48). Thus, it is expected that the ratio of wild type/wild type homodimers, wild type/mutant heterodimers, and mutant/mutant homodimers is 1:2:1 on cargo vesicles in KAND patients who have heterozygous mutations. To mimic the condition, we performed multimotor microtubule gliding assays with mixed types of motors (46, 49) (Fig. 8*A*). The velocity of wild type/mutant heterodimers and mutant/mutant homodimers was significantly reduced in the gliding assay (Fig. 8*B*), consistent with the results of our single-molecule assays (Figs. 3 and 7). Nest, we mixed wild type homodimers, wild type/mutant heterodimers, and mutant homodimers at 1:2:1. In the mixed condition, all three mutants inhibited the motility of wild-type KIF1A (Fig. 8*C*). As shown previously, the reduced concentration of KIF1A(wt) protein did not significantly affect the velocity in the gliding assay (*SI Appendix*, Fig. S8*A*) (46, 49, 50). Thus, the reduced velocity observed in the mixed condition is likely an inhibitory effect of mutant homodimers and heterodimers due to their reduced activities (Figs. 3 and 7). The microtubule gliding velocity showed 3 to 40% reduction, similar to the slower anterograde transport we observed in heterozygous worm neurons (Fig. 6*B*). Finally, to show that KAND mutations dominant negatively inhibit axonal transport in vivo, *unc-104(R9Q)*, *unc-104(R251Q)*, and *unc-104(P298L)* cDNA, corresponding to KIF1A(R11Q), KIF1A(R254Q), and KIF1A(P305L) mutants, were overexpressed in DA9 neuron (Fig. 8 *D*–*G* and *SI Appendix*, Fig. S8 *B* and *C*). As a result, in 70% UNC-104(R9Q)-, UNC-104(R251Q)-, and UNC-104(P298L)-expressed animals, synaptic vesicles misloclalized to the proximal region of the DA9 axon as well as dendrite (Fig. 8 *F* and *G* and *SI Appendix*, Fig. S8). No significant effects were observed in UNC-104(wild type)-overexpressed worms. These in vitro and in vivo data suggest that all three de novo KAND mutations analyzed in this study reduce axonal transport via a dominant-negative manner that reduces the ability of WT KIF1A motors to transport cargos with normal kinetics.

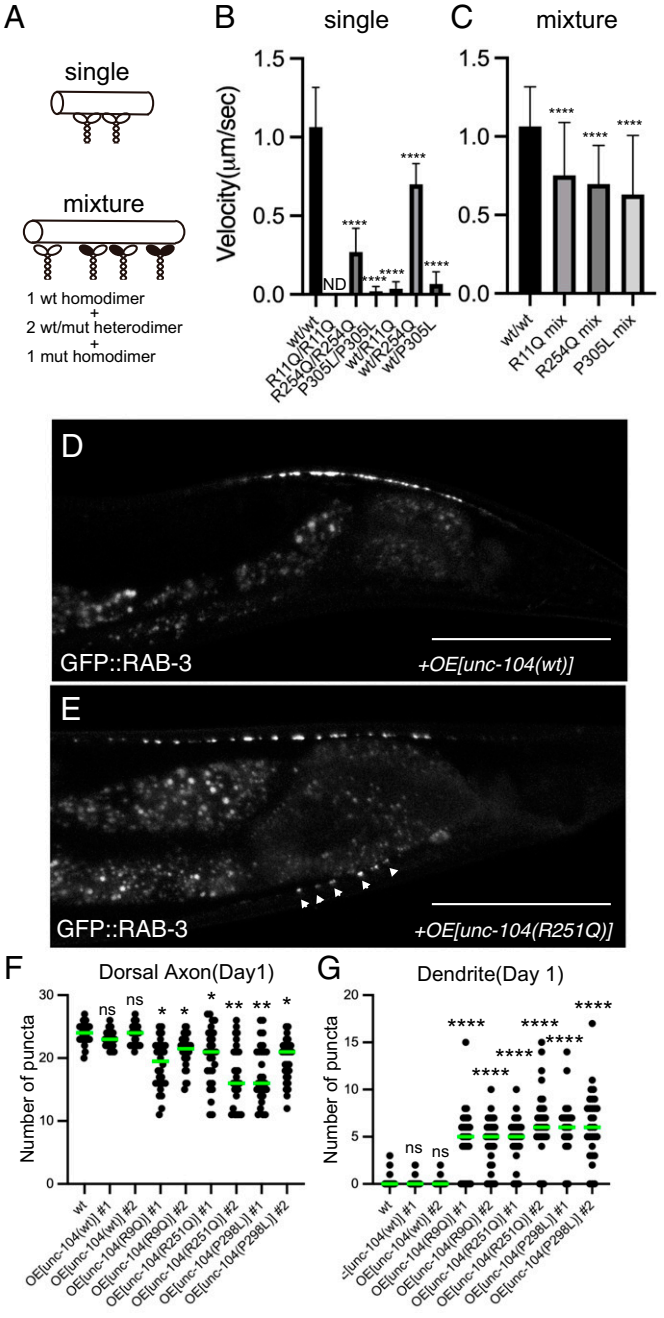


**Fig. 8.** Dominant-negative nature of KAND mutations. (*A*–*C*) Microtubule gliding assays. Schematic drawing of the microtubule gliding assay in different conditions (*A*). (*B*) Microtubule gliding assays using single motors. Bars and error bars represent mean and SD, respectively. $n$ = 146 (30 nM wt homodimers), 112 (30 nM R254Q homodimers), 20 (100 nM P305L homodimers), 59 (30 nM wt/R11Q heterodimers), 130 (30 nM wt/R254Q heterodimers), and 43 (30 nM wt/P305L heterodimers) microtubules from at least 3 independent experiments. Note that ND means no microtubule movement was observed in 100 nM KIF1A(R11Q) homodimers. Kruskal–Wallis test followed by Dunn;s multiple comparison test. ****, $P < 0.0001$. (*C*) Microtubule gliding assays using mixed motors. Bars and error bars represent mean and SD, respectively. $n$ = 146 (30 nM wt), 102 (30 nM R11Q mixture), 134 (30 nM R254Q mixture), and 108 (30 nM P305L mixture) microtubules. Kruskal–Wallis test followed by Dunn's multiple comparison test. ****, $P < 0.0001$. (*D*–*G*) UNC-104(wt), UNC-104(R9Q), UNC-104(R251Q), and UNC-104(P298L) were overexpressed in the wild-type background, and the localization of synaptic vesicles was observed. (*D* and *E*) Representative images showing the localization of synaptic vesicles in UNC-104(wt)-expressing worm (*D*) and UNC-104(R251Q)-expressing worm (*E*). Arrowheads show synaptic-vesicle-accumulated puncta that are mislocalized in the dendrite. Bars, 50 μm. (*F* and *G*) Dot plots showing the number of ventral axonal and dorsal dendritic puncta at 1 d. Each dot shows the number of puncta in the dorsal axon (*F*) and ventral dendrite (*G*) in each worm. Green bars represent median value. $n$ = 30 worms from each strain. Kruskal–Wallis test followed by Dunn's multiple comparison test. ns, adjusted $P$ value of >0.05 and no significant statistical difference. *, Adjusted $P$ value of <0.05. **, Adjusted $P$ value of <0.01. ****, Adjusted $P$ value of < 0.0001. See also *SI Appendix*, Fig. S8.

## Discussion

It is important to determine if heterozygous disease-associated phenotypes result from dominant-negative inhibition of biological processes or from haploinsufficiency of the affected genes because the difference significantly affects treatment strategies. Our data suggest de novo and autosomal dominant KAND mutations perturb axonal transport by two mechanisms. One inhibitory mechanism results from heterodimerization of mutant and wild-type KIF1A. Axonal transport motors alternately use two motor domains to move processively along microtubules (51). When a mutation in a motor protein gene is dominant and the mutation does not affect protein stability or expression, half of the motor dimers in the cell are predicted to be heterodimers composed of wild-type motor and mutant motor. Many disease-associated mutations in motor proteins are caused by autosomal dominant mutations; however, little attention has been paid to the properties of heterodimers in motor-associated diseases, and previous studies have mainly analyzed the properties of mutant homodimers in vitro (26, 27, 52–54). We show here that KAND mutations inhibit the motility of wild-type KIF1A by forming heterodimers. Another inhibitory effect by KAND mutations is caused when multiple KIF1A motors work as a team. In the axon, multiple KIF1A dimers are thought to bind to and cooperatively transport cargos (Fig. 9) (47, 48). Microtubule gliding assays performed using mixed motors show that cooperative transport is inhibited when KAND homodimers and heterodimers are mixed with wild-type KIF1A. In vivo, overexpression of KAND *unc-104* cDNAs dominant-negatively induces mislocalization of synaptic vesicles within the wild-type neuron (Fig. 8 *D*–*G*). Together with the data showing that *unc-104(R9Q)*/+, *unc-104(R251Q)*/+, and *unc-104(P298L)*/+ worms, but not *unc-104(null)*/+ worms, show defects in axonal transport, we suggest that these disease-associated mutations cause neuronal symptoms mainly through dominant-negative mechanisms (Fig. 9). In vitro assays revealed that the KIF1A(R11Q) motor does not move on microtubules at all, but KIF1A(R254Q) and KIF1A(P305L) motors do still move to some extent (Figs. 3 and 8*B*). Similar defects have been observed in the activity of mutant homodimers with other mutations (27). However, the degree of severity in some KAND patients, as well as model worms, are not always consistent with properties of mutant homodimers (27, 29, 30). This observation may be explained by the dominant-negative nature of mutations. This is partially supported by the microtubule gliding assay in which the difference in the mixed condition is much smaller than that of in single mutant homodimers (Fig. 8). Mutations in other axonal transport motors, such as KIF5A and cytoplasmic dynein, are causes of autosomal dominant neuropathies (52–55). We suggest that similar phenomena as observed here may underly the pathogenesis of these neuropathies.

We examined three human KIF1A mutations, namely, R11Q, R254Q, and P305L, in this study. It has been shown that KIF1A(P305) is in the L12 loop that supports the binding with microtubules (33). Consistent with this, we detected reduced microtubule binding in KIF1A(P305L) (Fig. 3). We show here that KIF1A(R11Q) reduces the binding frequency with microtubules, while KIF1A(R254Q) reduces run length (Fig. 3). This difference may arise because these two mutations affect different nucleotide states of KIF1A. KIF1A alternates between a strong binding state (ATP binding state) and a weak

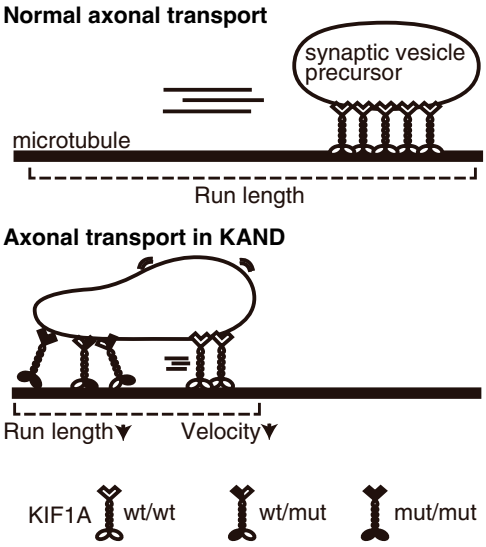


**Fig. 9.** Model schematic drawing showing how vesicular transport is suppressed in KAND patient axons. Not only mutant homodimers but also wild-type/mutant heterodimers inhibit axonal transport of synaptic vesicle precursors.

binding state (ADP binding state) with microtubules (12). R11 is at the terminal of the β1 sheet that stabilizes the ATP binding pocket, suggesting that the R11Q mutation might affect the ADP release or the binding of ATP. R254 is located within the L11 loop, which stabilizes the α4 helix, a positively charged microtubule-binding interface, in the weak binding state (ADP state) (56). Thus, the R254Q mutation might destabilize the α4 helix in the weak binding state (ADP state) and cause more frequent dissociation from microtubules during ATP hydrolysis, resulting to the shorter run lengths we observed. Consistent with these ideas, the microtubule binding affinity of KIF1A(R11Q) appears very weak, even in the presence of AMP-PNP (*SI Appendix*, Fig. S6). In contrast, the microtubule binding of KIF1A(R254Q) appears weaker than KIF1A(wt) in the presence of ADP but comparable to KIF1A(wt) in the presence of AMP-PNP (*SI Appendix*, Fig. S6). Because the suppressor mutation (D180N) reduces the negative charge on the motor surface, the mutation would strengthen the binding of KIF1A(R254Q) with microtubules, which might recover the run length (Fig. 4).

Multiple kinesin dimers cooperatively transport cargo vesicles. Force generation is fundamental to the cooperative transport (31, 46, 47). Thus, one concern is whether the single-molecule assays performed in unloaded conditions are relevant to the axonal transport of synaptic vesicle precursors. Microtubule gliding assays performed by mixed motors show the cooperative transport is inhibited by KAND motors (Fig. 8 *A*–*C*), suggesting that force generation is affected by KAND mutations. Unbiased genetic screening identified the *unc-104(D177N)* mutation recovers axonal transport in *unc-104(R251Q)* worms (Fig. 4 *A* and *B* and *SI Appendix*, Fig. S4). An orthologous mutation, KIF1A(D180N), recovered run length, landing rate, and velocity of human KIF1A(R254Q) in the single-molecule assay (Fig. 4 *C*–*G*). These suggest parameters measured by the single-molecule assay are relevant to the axonal transport in vivo while we cannot exclude that other physical parameters such as force generation are more directly relevant to the axonal transport.

It appears that almost all motor domain residues that are mutated in KAND are conserved in *C. elegans* UNC-104. In this study, we therefore assumed KAND mutations would similarly affect KIF1A and UNC-104. Measurement of UNC-104 would be required to directly test this hypothesis. However, at least in the case of the R254Q mutation, we find a beneficial mutation that recovers the motility of human KIF1A using model worms. Thus, worm models, including the three lines established in this work, will provide a foundation for future genetic and small-molecule screenings in the search for KAND treatment.

## Methods

**Worm Experiments.** *C. elegans* strains were maintained as described previously (57). N2 wild-type worms and OP50 feeder bacteria were obtained from the *C. elegans* genetic center (CGC). Transformation of *C. elegans* was performed by DNA injection as described (58). The swim test was performed as described previously (59). Time-lapse observation of axonal transport was performed as described (60).

**Genome Editing.** Target sequences for Cas9 and repair templates used to make *unc-104* mutants are described in *SI Appendix*, Table S1. Target sequences were inserted into pRB1017 (a gift from Andrew Fire, Stanford University, addgene #59936). pDD162 (a gift from Bob Goldstein, UNC Chapel Hill, addgene #47549) was used to express Cas9. These vectors and oligonucleotides were injected into young adult worms as described with a slight modification (36). Genotype was confirmed by PCR followed by Sanger sequencing.

**Strains.** Strains used in this study are described in *SI Appendix*, Table S2. Heterozygotes that have the *wyIs251* marker were generated by crossing *unc-104* homozygotes *wyIs251* males. Heterozygotes with wyIs85 markers were maintained by *mIn1* balancer. F1 worms showing nonunc phenotypes at the L4 stage were picked and transferred to new plates. Next day, adult worms were transferred to new plates (day 0). Worms were transferred to new plates until the observation.

**Statistical Analyses and Graph Preparation.** Statistical analyses were performed using Graph Pad Prism version 9. Statistical methods are described in the figure legends. Graphs were prepared using Graph Pad Prism version 9, exported in the TIFF format, and aligned by Adobe Illustrator 2021.

**Purification of Recombinant KIF1A.** Reagents were purchased from Nacarai tesque, unless described. Plasmids to express recombinant KIF1A are described in *SI Appendix*, Table S3. Proteins were expressed in BL21(DE3) and purified by Streptactin-XT resin (IBA Lifesciences) in the case of homodimers and Streptactin-XT resin and TALON resin (Takara Bio Inc.) in the case of heterodimers. Eluted fractions were further separated by an NGC chromatography system (Bio-Rad) equipped with a Superdex 200 Increase 10/300 GL column (Cytiva).

**TIRF Single-Molecule Motility Assays.** TIRF assays were performed as described (25). An ECLIPSE Ti2-E microscope equipped with a CFI Apochromat TIRF 100XC oil objective lens, an Andor iXion life 897 camera, and a Ti2-LAPP illumination system (Nikon) was used to observe single-molecule motility. NIS-Elements AR software version 5.2 (Nikon) was used to control the system.

**Data Availability.** All study data are included in the article and/or *SI Appendix*.

**ACKNOWLEDGMENTS.** Y.A. was supported by the Advanced Graduate Program for Future Medicine and Health Care, Tohoku University. K.H. was supported by JST PRESTO (Grant no. JPMJPR1877) and FRIS Creative Interdisciplinary Research Program, Tohoku University. S.N. was supported by JSPS KAKENHI (20H03247, 19H04738, 20K21378), the Naito Foundation, and the Uehara Foundation. Some worm strains and OP50 were obtained from the CGC. *unc-104(tm819)/mIn1* was obtained from the National Bioresource Project (NBRP). We thank Jeremy Allen, PhD, from Edanz (https://jp.edanz.com/acknowledgement?utm_source=ack&utm_medium=journal) for editing a draft of this manuscript.

Author affiliations: [a]Graduate School of Life Sciences, Tohoku University, Sendai, Miyagi 980-8578, Japan; [b]Department of Applied Physics, Graduate School of Engineering, Tohoku University, Sendai, Miyagi 980-8579, Japan; [c]Precursory Research for Embryonic Science and Technology (PRESTO), Japan Science and Technology Agency (JST), Saitama 332-0012, Japan; and [d]Frontier Research Institute for Interdisciplinary Sciences (FRIS), Tohoku University, Sendai, Miyagi 980-0845, Japan

1. N. Hirokawa, Y. Noda, Y. Tanaka, S. Niwa, Kinesin superfamily motor proteins and intracellular transport. *Nat. Rev. Mol. Cell Biol.* **10**, 682–696 (2009).
2. N. Hirokawa, S. Niwa, Y. Tanaka, Molecular motors in neurons: Transport mechanisms and roles in brain function, development, and disease. *Neuron* **68**, 610–638 (2010).
3. J. R. Kardon, R. D. Vale, Regulators of the cytoplasmic dynein motor. *Nat. Rev. Mol. Cell Biol.* **10**, 854–865 (2009).
4. R. D. Vale, T. S. Reese, M. P. Sheetz, Identification of a novel force-generating protein, kinesin, involved in microtubule-based motility. *Cell* **42**, 39–50 (1985).
5. Y. Tanaka *et al.*, Targeted disruption of mouse conventional kinesin heavy chain, kif5B, results in abnormal perinuclear clustering of mitochondria. *Cell* **93**, 1147–1158 (1998).
6. D. H. Hall, E. M. Hedgecock, Kinesin-related gene unc-104 is required for axonal transport of synaptic vesicles in C. elegans. *Cell* **65**, 837–847 (1991).
7. Y. Okada, H. Yamazaki, Y. Sekine-Aizawa, N. Hirokawa, The neuron-specific kinesin superfamily protein KIF1A is a unique monomeric motor for anterograde axonal transport of synaptic vesicle precursors. *Cell* **81**, 769–780 (1995).
8. S. Iwata, M. Morikawa, Y. Takei, N. Hirokawa, An activity-dependent local transport regulation via degradation and synthesis of KIF17 underlying cognitive flexibility. *Sci. Adv.* **6**, eabc8355 (2020).
9. J. E. Heuser, T. S. Reese, Evidence for recycling of synaptic vesicle membrane during transmitter release at the frog neuromuscular junction. *J. Cell Biol.* **57**, 315–344 (1973).
10. S. Niwa, Y. Tanaka, N. Hirokawa, KIF1Bbeta- and KIF1A-mediated axonal transport of presynaptic regulator Rab3 occurs in a GTP-dependent manner through DENN/MADD. *Nat. Cell Biol.* **10**, 1269–1279 (2008).
11. M. Kikkawa *et al.*, Switch-based mechanism of kinesin motors. *Nature* **411**, 439–445 (2001).
12. R. Nitta, M. Kikkawa, Y. Okada, N. Hirokawa, KIF1A alternately uses two loops to bind microtubules. *Science* **305**, 678–683 (2004).
13. O. I. Wagner *et al.*, Synaptic scaffolding protein SYD-2 clusters and activates kinesin-3 UNC-104 in C. elegans. *Proc. Natl. Acad. Sci. U.S.A.* **106**, 19605–19610 (2009).
14. D. R. Klopfenstein, R. D. Vale, The lipid binding pleckstrin homology domain in UNC-104 kinesin is necessary for synaptic vesicle transport in Caenorhabditis elegans. *Mol. Biol. Cell* **15**, 3729–3739 (2004).
15. R. Stucchi *et al.*, Regulation of KIF1A-driven dense core vesicle transport: $Ca^{2+}$/CaM controls DCV binding and liprin-α/TANC2 recruits DCVs to postsynaptic sites. *Cell Rep.* **24**, 685–700 (2018).
16. D. T. Byrd *et al.*, UNC-16, a JNK-signaling scaffold protein, regulates vesicle transport in C. elegans. *Neuron* **32**, 787–800 (2001).
17. Q. Zheng *et al.*, The vesicle protein SAM-4 regulates the processivity of synaptic vesicle transport. *PLoS Genet.* **10**, e1004644 (2014).
18. S. Yogev, R. Cooper, R. Fetter, M. Horowitz, K. Shen, Microtubule organization determines axonal transport dynamics. *Neuron* **92**, 449–460 (2016).
19. M. P. Klassen *et al.*, An Arf-like small G protein, ARL-8, promotes the axonal transport of presynaptic cargoes by suppressing vesicle aggregation. *Neuron* **66**, 710–723 (2010).
20. S. P. Koushika *et al.*, Mutations in Caenorhabditis elegans cytoplasmic dynein components reveal specificity of neuronal retrograde cargo. *J. Neurosci.* **24**, 3907–3916 (2004).
21. J. Kumar *et al.*, The Caenorhabditis elegans Kinesin-3 motor UNC-104/KIF1A is degraded upon loss of specific binding to cargo. *PLoS Genet.* **6**, e1001200 (2010).
22. S. Niwa *et al.*, Autoinhibition of a neuronal kinesin UNC-104/KIF1A regulates the size and density of synapses. *Cell Rep.* **16**, 2129–2141 (2016).
23. S. Niwa *et al.*, BORC regulates the axonal transport of synaptic vesicle precursors by activating ARL-8. *Curr. Biol.* **27**, 2569–2578.e4 (2017).
24. A. J. Otsuka *et al.*, The C. elegans unc-104 gene encodes a putative kinesin heavy chain-like protein. *Neuron* **6**, 113–122 (1991).
25. K. Chiba *et al.*, Disease-associated mutations hyperactivate KIF1A motility and anterograde axonal transport of synaptic vesicle precursors. *Proc. Natl. Acad. Sci. U.S.A.* **116**, 18429–18434 (2019).
26. S. Esmaeeli Nieh *et al.*, De novo mutations in KIF1A cause progressive encephalopathy and brain atrophy. *Ann. Clin. Transl. Neurol.* **2**, 623–635 (2015).
27. L. Boyle *et al.*, Genotype and defects in microtubule-based motility correlate with clinical severity in KIF1A-associated neurological disorder. *HGG Adv.* **2**, 100026 (2021).
28. M. Morikawa *et al.*, A neuropathy-associated kinesin KIF1A mutation hyper-stabilizes the motor-neck interaction during the ATPase cycle. *EMBO J.* **41**, e108899 (2022).
29. T. Nemani *et al.*; Genomics England Research Consortium, KIF1A-related disorders in children: A wide spectrum of central and peripheral nervous system involvement. *J. Peripher. Nerv. Syst.* **25**, 117–124 (2020).
30. C. Ohba *et al.*, De novo KIF1A mutations cause intellectual deficit, cerebellar atrophy, lower limb spasticity and visual disturbance. *J. Hum. Genet.* **60**, 739–742 (2015).
31. B. G. Budaitis *et al.*, Pathogenic mutations in the kinesin-3 motor KIF1A diminish force generation and movement through allosteric mechanisms. *J. Cell Biol.* **220**, e202004227 (2021).
32. P. Guedes-Dias *et al.*, Kinesin-3 responds to local microtubule dynamics to target synaptic cargo delivery to the presynapse. *Curr. Biol.* **29**, 268–282.e8 (2019).
33. A. J. Lam *et al.*, A highly conserved $3_{10}$ helix within the kinesin motor domain is critical for kinesin function and human health. *Sci. Adv.* **7**, eabf1002 (2021).
34. C. Aguilera *et al.*, The novel KIF1A missense variant (R169T) strongly reduces microtubule stimulated ATPase activity and is associated with NESCAV syndrome. *Front. Neurosci.* **15**, 618098 (2021).
35. M. Tomishige, D. R. Klopfenstein, R. D. Vale, Conversion of Unc104/KIF1A kinesin into a processive motor after dimerization. *Science* **297**, 2263–2267 (2002).
36. J. A. Arribere *et al.*, Efficient marker-free recovery of custom genetic modifications with CRISPR/Cas9 in Caenorhabditis elegans. *Genetics* **198**, 837–846 (2014).
37. M. P. Klassen, K. Shen, Wnt signaling positions neuromuscular connectivity by inhibiting synapse formation in C. elegans. *Cell* **130**, 704–716 (2007).
38. C. I. Maeder, A. San-Miguel, E. Y. Wu, H. Lu, K. Shen, In vivo neuron-wide analysis of synaptic vesicle precursor trafficking. *Traffic* **15**, 273–291 (2014).
39. R. D. Vale *et al.*, Direct observation of single kinesin molecules moving along microtubules. *Nature* **380**, 451–453 (1996).
40. R. J. McKenney, W. Huynh, M. E. Tanenbaum, G. Bhabha, R. D. Vale, Activation of cytoplasmic dynein motility by dynactin-cargo adapter complexes. *Science* **345**, 337–341 (2014).
41. Y. Okada, N. Hirokawa, A processive single-headed motor: Kinesin superfamily protein KIF1A. *Science* **283**, 1152–1157 (1999).
42. J. Yan *et al.*, Kinesin-1 regulates dendrite microtubule polarity in Caenorhabditis elegans. *eLife* **2**, e00133 (2013).
43. S. T. Brady, K. K. Pfister, G. S. Bloom, A monoclonal antibody against kinesin inhibits both anterograde and retrograde fast axonal transport in squid axoplasm. *Proc. Natl. Acad. Sci. U.S.A.* **87**, 1061–1065 (1990).
44. A. Uchida, N. H. Alami, A. Brown, Tight functional coupling of kinesin-1A and dynein motors in the bidirectional transport of neurofilaments. *Mol. Biol. Cell* **20**, 4997–5006 (2009).
45. S. Ally, A. G. Larson, K. Barlan, S. E. Rice, V. I. Gelfand, Opposite-polarity motors activate one another to trigger cargo transport in live cells. *J. Cell Biol.* **187**, 1071–1082 (2009).
46. Q. Feng, K. J. Mickolajczyk, G. Y. Chen, W. O. Hancock, Motor reattachment kinetics play a dominant role in multimotor-driven cargo transport. *Biophys. J.* **114**, 400–409 (2018).
47. S. R. Norris *et al.*, A method for multiprotein assembly in cells reveals independent action of kinesins in complex. *J. Cell Biol.* **207**, 393–406 (2014).
48. K. Hayashi, S. Hasegawa, T. Sagawa, S. Tasaki, S. Niwa, Non-invasive force measurement reveals the number of active kinesins on a synaptic vesicle precursor in axonal transport regulated by ARL-8. *Phys. Chem. Chem. Phys.* **20**, 3403–3410 (2018).
49. B. Ebbing *et al.*, Effect of spastic paraplegia mutations in KIF5A kinesin on transport activity. *Hum. Mol. Genet.* **17**, 1245–1252 (2008).
50. F. Gibbons, J. F. Chauwin, M. Despósito, J. V. José, A dynamical model of kinesin-microtubule motility assays. *Biophys. J.* **80**, 2515–2526 (2001).
51. R. D. Vale, The molecular motor toolbox for intracellular transport. *Cell* **112**, 467–480 (2003).
52. J. Nakano, K. Chiba, S. Niwa, An ALS-associated KIF5A mutant forms oligomers and aggregates and induces neuronal toxicity. *Genes Cells* **27**, 421–435 (2022).
53. M. G. Marzo *et al.*, Molecular basis for dyneinopathies reveals insight into dynein regulation and dysfunction. *eLife* **8**, e47246 (2019).
54. H. T. Hoang, M. A. Schlager, A. P. Carter, S. L. Bullock, DYNC1H1 mutations associated with neurological diseases compromise processivity of dynein-dynactin-cargo adaptor complexes. *Proc. Natl. Acad. Sci. U.S.A.* **114**, E1597–E1606 (2017).
55. E. Reid *et al.*, A kinesin heavy chain (KIF5A) mutation in hereditary spastic paraplegia (SPG10). *Am. J. Hum. Genet.* **71**, 1189–1194 (2002).
56. M. Kikkawa, N. Hirokawa, High-resolution cryo-EM maps show the nucleotide binding pocket of KIF1A in open and closed conformations. *EMBO J.* **25**, 4187–4194 (2006).
57. S. Brenner, The genetics of Caenorhabditis elegans. *Genetics* **77**, 71–94 (1974).
58. C. C. Mello, J. M. Kramer, D. Stinchcomb, V. Ambros, Efficient gene transfer in C. elegans: Extrachromosomal maintenance and integration of transforming sequences. *EMBO J.* **10**, 3959–3970 (1991).
59. J. T. Pierce-Shimomura *et al.*, Genetic analysis of crawling and swimming locomotory patterns in C. elegans. *Proc. Natl. Acad. Sci. U.S.A.* **105**, 20982–20987 (2008).
60. Y. Anazawa, S. Niwa, Analyzing the impact of gene mutations on axonal transport in Caenorhabditis elegans. *Methods Mol. Biol.* **2431**, 465–479 (2022).